

# Coherent dynamics of a flux qubit coupled to a harmonic oscillator

I. Chiorescu,<sup>1,\*</sup> P. Bertet,<sup>1</sup> K. Semba,<sup>1,2</sup> Y. Nakamura,<sup>1,3</sup> C.J.P.M. Harmans,<sup>1</sup> and J.E. Mooij<sup>1</sup>

<sup>1</sup>*Quantum Transport group, Kavli Institute of Nanoscience,  
Delft University of Technology, 2628 CJ, Delft, Netherlands*

<sup>2</sup>*NTT Basic Research Laboratories, 3-1 Morinosato-Wakamiya, Atsugi, 243-0198, Japan*

<sup>3</sup>*NEC Fundamental Research Laboratories, 34 Miyukigaoka, Tsukuba, Ibaraki 305-8501, Japan*

(Dated: Nature. Received 25 May; accepted 5 July 2004. doi:10.1038/nature02831)

In the emerging field of quantum computation<sup>1</sup> and quantum information, superconducting devices are promising candidates for the implementation of solid-state quantum bits or qubits. Single-qubit operations<sup>2–6</sup>, direct coupling between two qubits<sup>7–10</sup>, and the realization of a quantum gate<sup>11</sup> have been reported. However, complex manipulation of entangled states – such as the coupling of a two-level system to a quantum harmonic oscillator, as demonstrated in ion/atom-trap experiments<sup>12,13</sup> or cavity quantum electrodynamics<sup>14</sup> – has yet to be achieved for superconducting devices. Here we demonstrate entanglement between a superconducting flux qubit (a two-level system) and a superconducting quantum interference device (SQUID). The latter provides the measurement system for detecting the quantum states; it is also an effective inductance that, in parallel with an external shunt capacitance, acts as a harmonic oscillator. We achieve generation and control of the entangled state by performing microwave spectroscopy and detecting the resultant Rabi oscillations of the coupled system.

The device was realized by electron-beam lithography and metal evaporation. The qubit-SQUID geometry is shown in Fig. 1a: a large loop interrupted by two Josephson junctions (the SQUID) is merged with the smaller loop on the right-hand side comprising three in-line Josephson junctions (the flux qubit)<sup>15</sup>. By applying a perpendicular external magnetic field, the qubit is biased around  $\Phi_0/2$ , where  $\Phi_0 = h/2e$  is the flux quantum. Previous spectroscopy<sup>16</sup> and coherent time-domain experiments<sup>6</sup> have shown that the flux qubit is a controllable two-level system with ‘spin-up/spin-down’ states corresponding to persistent currents flowing in ‘clockwise/anticlockwise’ directions and coupled by tunneling. Here we show that a stronger qubit–SQUID coupling allows us to investigate the coupled dynamics of a ‘qubit–harmonic oscillator’ system.

The qubit Hamiltonian is defined by the charging and Josephson energy of the qubit outer junctions ( $E_C = e^2/2C$  and  $E_J = hI_C/4e$  where  $C$  and  $I_C$  are their capacitance and critical current)<sup>16</sup>. In a two-level truncation, the Hamiltonian becomes  $H_q/h = -\epsilon\sigma_z/2 - \Delta\sigma_x/2$  where  $\sigma_{z,x}$  are the Pauli matrices in the spin-up/spin-down basis,  $\Delta$  is the tunnel splitting and  $\epsilon \cong I_p\Phi_0(\gamma_q - \pi)/h\pi$  ( $I_p$  is the qubit maximum persistent current and  $\gamma_q$  is the superconductor phase across the three junctions).

The resulting energy level spacing represents the qubit Larmor frequency  $F_L = \sqrt{\Delta^2 + \epsilon^2}$ . The SQUID dynamics is characterized by the Josephson inductance of the junctions  $L_J \approx 80$  pH, shunt capacitance  $C_{sh} \approx 12$  pF (see Fig. 1a) and self-inductances  $L_{sl} \approx 170$  pH of the SQUID and shunt-lines. In our experiments, the SQUID circuit behaves like a harmonic oscillator described by  $H_{sq} = h\nu_p(a^\dagger a + 1/2)$ , where  $2\pi\nu_p = 1/\sqrt{(L_J + L_{sl})C_{sh}}$  is called the plasma frequency and  $a$  ( $a^\dagger$ ) is the plasmon annihilation (creation) operator. Henceforth  $|\beta n\rangle$  represents the state with the qubit in the ground ( $\beta = 0$ ) or excited ( $\beta = 1$ ) level, and the oscillator on the  $n^{\text{th}}$  level ( $n = 0, 1, 2, \dots$ ). The corresponding level diagram is sketched in Fig. 1b (inset). The coupling between the qubit and the oscillator originates from the current distribution in the shared branches (Fig. 1a) and gives rise to an interaction Hamiltonian  $H_{q-sq} = \lambda\sigma_z(a + a^\dagger)$  with  $\lambda \approx 0.2$  GHz in our device<sup>17</sup> (the estimated qubit-SQUID coupling is  $M \approx 20$  pH).

Measurements are performed at  $T=25$  mK using low-noise circuitry to minimize decoherence, relaxation and thermal activation. The system is first initialized by allowing it to relax to the  $|00\rangle$  ground state. With successive resonant microwave pulses we achieve controlled superposition of various  $|\beta n\rangle$  states, as shown below. The readout<sup>6</sup> is performed by applying a short current pulse  $I_b$  ( $\sim 30$  ns) and by monitoring whether the SQUID switches to the finite-voltage state. After averaging typically 10000 readouts, we obtain the probability  $P_{sw}(I_b)$  which for properly-chosen parameters is proportional to the excited state occupancy. In the following, we first show the spectroscopy of the coupled qubit–oscillator system and Rabi oscillations of the qubit. Next we demonstrate coherent dynamics of the coupled system.

We performed spectroscopy of the coupled qubit–oscillator system by applying a long (300 ns) microwave pulse with various frequencies and measuring the SQUID switching probability. Peaks and dips are observed and their resonant frequencies as a function of  $\Delta\Phi = \Phi_{ext} - \Phi_0/2$  are given in Fig. 1b. We obtain one manifold of three resonances spaced by  $\sim 2.91$  GHz. This frequency coincides with the designed oscillator eigenfrequency  $\nu_p$ . In addition, we observe a spectroscopic peak or dip that depends only weakly on the magnetic field (circles in Fig. 1b). For lower microwave power, only the qubit band (squares) remains visible. A numerical

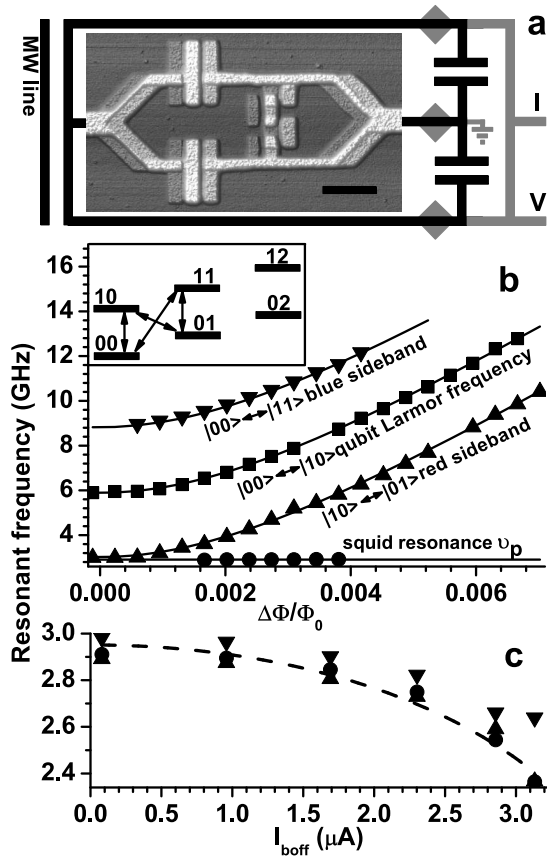


FIG. 1: Qubit–SQUID device and spectroscopy **a**, Atomic force micrograph of the SQUID (large loop) merged with the flux qubit (the smallest loop closed by three junctions); the qubit to SQUID area ratio is 0.37. Scale bar,  $1\mu\text{m}$ . The SQUID (qubit) junctions have a critical current of  $4.2$  ( $0.45$ )  $\mu\text{A}$ . The device is made of aluminium by two symmetrically angled evaporations with an oxidation step in between. The surrounding circuit shows aluminium shunt capacitors and lines (in black) and gold quasiparticle traps<sup>3</sup> and resistive leads (in grey). The microwave field is provided by the shortcut of a coplanar waveguide (MW line) and couples inductively to the qubit. The current line ( $I$ ) delivers the readout pulses, and the switching event is detected on the voltage line ( $V$ ). **b**, Resonant frequencies indicated by peaks in the SQUID switching probability when a long microwave pulse excites the system before the readout pulse. Data are represented as a function of the external flux through the qubit area away from the qubit symmetry point. Inset, energy levels of the qubit–oscillator system for some given bias point. The blue and red sidebands are shown by down- and up-triangles, respectively; continuous lines are obtained by adding  $2.96$  GHz and  $-2.90$  GHz, respectively, to the central continuous line (numerical fit). These values are close to the oscillator resonance  $\nu_p$  at  $2.91$  GHz (solid circles) and we attribute the small differences to the slight dependence of  $\nu_p$  on qubit state. **c**, The plasma resonance (circles) and the distances between the qubit peak (here  $F_L = 6.4$  GHz) and the red/blue (up/down triangles) sidebands as a function of an offset current  $I_{boff}$  through the SQUID. The data are close to each other and agree well with the theoretical prediction for  $\nu_p$  versus offset current (dashed line).

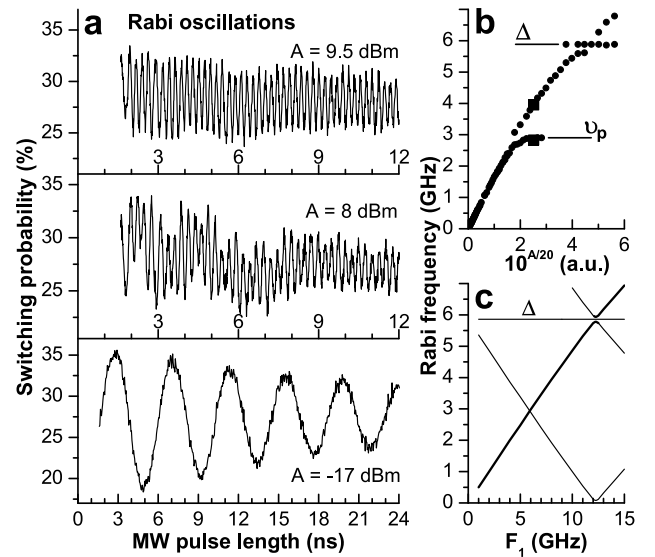


FIG. 2: Rabi oscillations at the qubit symmetry point  $\Delta = 5.9$  GHz. **a**, Switching probability as a function of the microwave pulse length for three microwave nominal powers; decay times are of the order of  $25$  ns. For  $A = 8$  dBm, bi-modal beatings are visible (the corresponding frequencies are shown by the filled squares in **b**). **b**, Rabi frequency, obtained by fast Fourier transformation of the corresponding oscillations, versus microwave amplitude. In the weak driving regime, the linear dependence is in agreement with estimations based on sample design. A first splitting appears when the Rabi frequency is  $\sim \nu_p$ . In the strong driving regime, the power independent Larmor precession at frequency  $\Delta$  gives rise to a second splitting. **c**, This last aspect is obtained in numerical simulations where the microwave driving is represented by a term  $(1/2)\hbar F_1 \cos(\Delta t)$  and a small deviation from the symmetry point ( $100$  MHz) is introduced in the strong driving regime (the thick line indicates the main Fourier peaks). Radiative shifts<sup>20</sup> at high microwave power could account for such a shift in the experiment.

fit (continuous line) of this band leads to  $E_J = 225$  GHz,  $E_C = 7.3$  GHz, and ratio of area of qubit junctions  $\alpha = 0.76$  ( $\Delta = 5.9$  GHz,  $I_p = 275$  nA). The appearance of the manifold instead of a single resonance is due to the qubit coupling with the oscillator mode  $\nu_p$  (ref. 18). Similarly to atomic physics, we call the  $|00\rangle$  to  $|11\rangle$  ( $|01\rangle$  to  $|10\rangle$ ) transitions the blue (red) sidebands (see the ladder energy diagram of the  $|\beta n\rangle$  states in Fig. 1b inset). We note that near the qubit symmetry point, the closeness of the oscillator resonance and the red sideband, visible owing to a small thermal occupation of the  $|01\rangle$  state, is purely accidental. To verify that the oscillator involved is indeed the SQUID plasma mode, we repeated the above measurements in the presence of an offset bias current  $I_{boff}$  which decreases the plasma frequency following<sup>19</sup>  $\nu_p(1 - (I_{boff}/I_c)^2)^{1/4}$ , where  $I_c$  is the SQUID critical current ( $4.2$  A). The data in Fig. 1c show the distance between the qubit peak for

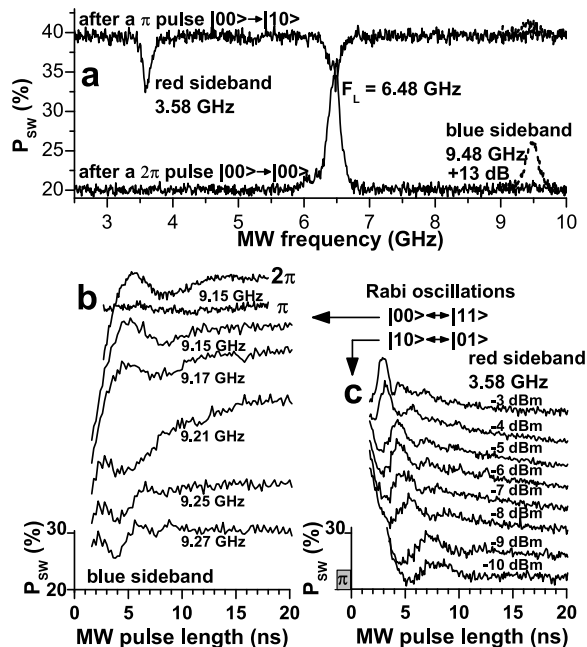


FIG. 3: Generation and control of entangled states. **a**, Spectroscopic characterization of the energy levels (see Fig. 1b inset) after a  $\pi$  (upper scan) and a  $2\pi$  (lower scan) Rabi pulse on the qubit transition. In the upper scan, the system is first excited to  $|10\rangle$  from which it decays towards the  $|01\rangle$  excited state (red sideband at 3.58 GHz) or towards the  $|00\rangle$  ground state ( $F_L = 6.48$  GHz). In the lower scan, the system is rotated back to the initial state  $|00\rangle$  wherefrom it is excited into the  $|10\rangle$  or  $|11\rangle$  states (see, in dashed, the blue sideband peak at 9.48 GHz for 13 dB more power). **b**, Coupled Rabi oscillations: the blue sideband is excited and the switching probability is recorded as a function of the pulse length for different microwave powers (plots are shifted vertically for clarity). For large microwave powers, the resonance peak of the blue sideband is shifted to 9.15 GHz. When detuning the microwave excitation away from resonance, the Rabi oscillations become faster (bottom four curves). These oscillations are suppressed by preparing the system in the  $|10\rangle$  state with a  $\pi$  pulse and revived after a  $2\pi$  pulse (top two curves in Fig. 3b). **c**, Coupled Rabi oscillations: after a  $\pi$  pulse on the qubit resonance ( $|00\rangle \rightarrow |10\rangle$ ) we excite the red sideband at 3.58 GHz. The switching probability shows coherent oscillations between the states  $|10\rangle$  and  $|01\rangle$ , at various microwave powers (the curves are shifted vertically for clarity). The decay time of the coherent oscillations in **a**, **b** is  $\sim 3$  ns.

$F_L = 6.4$  GHz and the blue/red sidebands (down/up triangles) that decreases together with the oscillator resonance (circles).

To realize quantum operations on the qubit only, we apply a resonant microwave pulse with frequency  $F_{mw} = F_L$ . The operation is performed at the qubit symmetry point  $\gamma_q = \pi$  where  $F_L = \Delta$ . In Fig. 2a, the SQUID switching probability is plotted against the microwave pulse length for three microwave power levels. The ob-

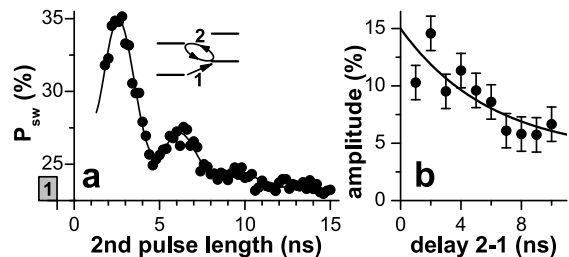


FIG. 4: Oscillator relaxation time. **a**, Rabi oscillations between the  $|01\rangle$  and  $|10\rangle$  states (during pulse 2 in the inset) obtained after applying a first pulse (1) in resonance with the oscillator transition. Here, the interval between the two pulses is 1 ns. The continuous line represents a fit using an exponentially decaying sinusoidal oscillation plus an exponential decay of the background (due to the relaxation into the ground state). The oscillation's decay time is  $\tau_{coh} = 2.9$  ns, whereas the background decay time is  $\sim 4$  ns. **b**, The amplitude of Rabi oscillations as a function of the interval between the two pulses (the vertical bars represent standard error bars estimated from the fitting procedure, see **a**). Owing to the oscillator relaxation, the amplitude decays in  $\tau_{rel} \approx 6$  ns (the continuous line represents an exponential fit).

served Rabi oscillations decay within  $\sim 30$  ns. Remarkably, we can reach Rabi frequencies comparable to the Larmor frequency (up to 6.6 GHz). Using Fourier transformation, we extract the Rabi frequency as a function of the microwave amplitude (Fig. 2b). In the weak driving regime, the Rabi frequency increases linearly with the microwave power, as expected<sup>6</sup>. Near the oscillator resonance  $\nu_p$ , we see two frequencies in the spectrum, a behaviour which is probably caused by the qubit–oscillator coupling. At even higher microwave powers, the spectrum exhibits again a second frequency component at  $\Delta$ . A qualitatively similar behaviour is also obtained in numerical simulations (see Fig. 2c) when we consider the qubit driven by an additional term  $(1/2)\hbar F_1 \cos(\Delta t)$  in  $H_q$  ( $F_1$  and  $\Delta$  are the microwave amplitude and frequency, respectively).

We now turn to the conditional dynamics resulting from the qubit–oscillator coupling. We first determine the blue and red sideband resonant frequencies by spectroscopic means using a two-pulse sequence (Fig. 3a). The qubit is prepared in the excited state by a  $\pi$  pulse at the Larmor frequency. A second pulse (18 ns) of variable frequency induces resonant qubit de-excitation (dips in Fig. 3a top trace) marking the red sideband and the Larmor frequency. Similarly, after a  $2\pi$  pulse which places the qubit in its ground state, we search for resonant excitations (peaks in Fig. 3a bottom trace) that mark the Larmor frequency and the blue sideband. No resonance is seen on the red sideband, showing that the oscillator is in its ground state with a large probability. Note that in order to excite the blue sideband, we have to increase the microwave power by at least 10 dB, probably due to

less effective microwave transmission in the 8 – 9 GHz range (note also the absence of spectroscopy peaks in this frequency range in Fig. 1b). At high microwave powers, we observe radiative shifts<sup>20</sup> of the resonances. We now exploit these resonances to study the dynamics of the coupled system by applying pulses of varying length. In Fig. 3b, Rabi oscillations are shown for the  $|00\rangle$  to  $|11\rangle$  transition. When the microwave frequency is detuned from resonance, the Rabi oscillations are accelerated (bottom four curves, to be compared with the fifth curve). After a  $\pi$  pulse which prepares the system in the  $|10\rangle$  state, these oscillations are suppressed (second curve in Fig. 3b). After a  $2\pi$  pulse they are revived (first curve in Fig. 3b). In the case of Fig. 3c, the qubit is first excited onto the  $|10\rangle$  state by a  $\pi$  pulse and a second pulse in resonance with the red sideband transition drives the system between the  $|10\rangle$  and  $|01\rangle$  states. The Rabi frequency depends linearly on the microwave amplitude, with a smaller slope compared to the bare qubit driving. During the time evolution of the coupled Rabi oscillations shown in Figs. 3b and 3c, the qubit and the oscillator experience a time-dependent entanglement, although the present data do not permit us to quantify it to a sufficient degree of confidence.

The sideband Rabi oscillations of Fig. 3 show a short coherence time ( $\sim 3$  ns) which we attribute mostly to the oscillator relaxation. To determine its relaxation time, we performed the following experiment. First, we excite the oscillator with a resonant low power microwave pulse. After a variable delay  $\Delta t$ , during which the oscillator relaxes towards  $n = 0$ , we start recording Rabi oscillations on the red sideband transition (see Fig. 4a for  $\Delta t = 1$  ns). The decay of the oscillation amplitude as a function of  $\Delta t$  corresponds to an oscillator relaxation time of  $\sim 6$  ns (Fig. 4b), consistent with a quality factor of 100 – 150 estimated from the width of the  $\nu_p$  resonance. The exponential fit (continuous line in Fig. 4b) shows an offset of  $\sim 4\%$  due to thermal effects. To estimate the higher bound of the sample temperature, we consider that the visibility of the oscillations presented here (Figs. 2-4) is set by the detection efficiency and not by the state preparation. When related to the maximum signal of the qubit Rabi oscillations of  $\sim 40\%$ , the 4%-offset corresponds to  $\sim 10\%$  thermal occupation of oscillator excited states (an effective temperature of  $\sim 60$  mK). Consistently, we also observe low-amplitude red sideband oscillations without preliminary microwave excitation of the oscillator.

We have demonstrated coherent dynamics of a coupled superconducting two-level plus harmonic oscillator system, implying that the two subsystems are entangled. Increasing the coupling strength and the oscillator relaxation time should allow us to quantify the entanglement, as well as to study non-classical states of the oscillator. Our results provide strong indications that solid-state quantum devices could in future be used as elements for the manipulation of quantum information.

We thank A. Blais, G. Burkard, D. DiVincenzo, G. Falci, M. Grifoni, S. Lloyd, S. Miyashita, T. Orlando, R. N. Schouten, L. Vandersypen, F. K. Wilhelm for discussions. This work was supported by the Dutch Foundation for Fundamental Research on Matter (FOM), the E.U. Marie Curie and SQUBIT grants, and the U.S. Army Research Office. The authors declare that they have no competing financial interests. Correspondence and requests for materials should be addressed to I.C. (e-mail: chiorescu@pa.msu.edu) and J.E.M. (email: mooij@qt.tn.tudelft.nl).

---

\* Present address: Department of Physics and Astronomy, Michigan State University, East Lansing, Michigan 48824, USA

- [1] Nielsen, M. A., Chuang, I. L. *Quantum Computation and Quantum Information* (Cambridge Univ. Press, Cambridge, 2000).
- [2] Nakamura, Y. *et al.* Coherent control of macroscopic quantum states in a single-Cooper-pair box. *Nature* **398**, 786-788 (1999).
- [3] Vion, D. *et al.* Manipulating the quantum state of an electrical circuit. *Science* **296**, 886-889 (2002).
- [4] Yu, Y., Han, S., Chu, X., Chu, S., Wang, Z. Coherent temporal oscillations of macroscopic quantum states in a Josephson junction. *Science* **296**, 889-892 (2002).
- [5] Martinis, J. M., Nam, S., Aumentado, J., Urbina, C., Rabi oscillations in a large Josephson-junction qubit. *Phys. Rev. Lett.* **89**, 117901 (2002).
- [6] Chiorescu, I., Nakamura, Y., Harmans, C. J. P. M., Mooij, J. E. Coherent quantum dynamics of a superconducting flux qubit. *Science* **299**, 1869-1871 (2003).
- [7] Pashkin, Yu. A., *et al.* Quantum oscillations in two coupled charge qubits. *Nature* **421**, 823-826 (2003).
- [8] Berkley, A. J., *et al.* Entangled macroscopic quantum states in two superconducting qubits. *Science* **300**, 1548-1550 (2003).
- [9] Majer, J. B., Paauw, F. G., ter Haar, A. C. J., Harmans, C. J. P. M., Mooij, J. E. Spectroscopy on two coupled flux qubits. Preprint at <http://arxiv.org/abs/cond-mat/0308192> (2003).
- [10] Izmalkov, A., *et al.* Experimental evidence for entangled states formation in a system of two coupled flux qubits. Preprint at <http://arxiv.org/abs/cond-mat/0312332> (2003).
- [11] Yamamoto, T., Pashkin, Yu. A., Astafiev, O., Nakamura, Y., Tsai, J. S. Demonstration of conditional gate operation using superconducting charge qubits. *Nature* **425**, 941-944 (2003).
- [12] Leibfried, D., Blatt, R., Monroe, C., Wineland, D., Quantum dynamics of single trapped ions. *Rev. Mod. Phys.* **75**, 281-324 (2003).
- [13] Mandel, O., *et al.* Controlled collisions for multi-particle entanglement of optically trapped atoms. *Nature* **425**, 937-940 (2003).
- [14] Raimond, J.M., Brune, M., Haroche, S. Manipulating quantum entanglement with atoms and photons in a cavity. *Rev. Mod. Phys.* **73**, 565-582 (2001).
- [15] Mooij, J. E., *et al.* Josephson Persistent-Current Qubit.

- Science* **285**, 1036-1039 (1999).
- [16] van der Wal, C. H., *et al.* Quantum superposition of macroscopic persistent-current states. *Science* **290**, 773-777 (2000).
- [17] Burkard, G., *et al.* Asymmetry and decoherence in double-layer persistent-current qubit. Preprint at <<http://arxiv.org/abs/cond-mat/0405273>> (2004).
- [18] Goorden, M.C., Thorwart, M., Grifoni, M. Entanglement spectroscopy of a driven solid-state qubit and its detector. Preprint at <<http://arxiv.org/abs/cond-mat/0405220>> (2004).
- [19] Tinkham, M., *Introduction to superconductivity* 2nd edn (McGraw-Hill, New York, 1996), pp. 207.
- [20] Cohen-Tannoudji, C., Dupont-Roc, J., Grynberg, G. *Atom-photon interactions: basic processes and applications* Ch. II E (John Wiley & Sons, New York, 1992).